ACS APPLIED MATERIALS & INTERFACES

www.acsami.org

Research Article

Earth-Abundant Kaolinite Nanoplatelet Gel Electrolytes for Solid-State Lithium Metal Batteries

Cory M. Thomas,[⊥] Davy Zeng,[⊥] Hsien Cheng Huang, Thang Pham, Carlos G. Torres-Castanedo, Michael J. Bedzyk, Vinayak P. Dravid, and Mark C. Hersam*

Cite This: *ACS Appl. Mater. Interfaces* 2024, 16, 34913−34922

ABSTRACT: Lithium-ion batteries are the leading energy storage technology for portable electronics and vehicle electrification. However, demands for enhanced energy density, safety, and scalability necessitate solid-state alternatives to traditional liquid electrolytes. Moreover, the rapidly increasing utilization of lithium-ion batteries further requires that next-generation electrolytes are derived from earth-abundant raw materials in order to minimize supply chain and environmental concerns. Toward these ends, clay-based nanocomposite electrolytes hold significant promise since they utilize earth-abundant materials that possess superlative mechanical, thermal, and electrochemical stability, which suggests their compatibility with energy-dense lithium metal anodes. Despite these advantages, nanocomposite electrolytes rarely employ kaolinite, the most abundant variety of clay, due to strong interlayer interactions that have historically precluded efficient exfoliation of kaolinite. Overcoming this limitation, here we demonstrate a scalable liquid-phase exfoliation process that produces kaolinite nanoplatelets (KNPs) with high gravimetric surface area, thus enabling the formation of mechanically robust nanocomposites. In particular, KNPs are combined with a succinonitrile (SN) liquid electrolyte to form a nanocomposite gel electrolyte with high room-temperature ionic conductivity (1 mS cm^{-1}), stiff storage modulus (>10 MPa), wide electrochemical stability window (4.5 V vs Li/Li^+), and excellent thermal stability (>100 °C). The resulting KNP-SN nanocomposite gel electrolyte is shown to be suitable for high-rate rechargeable lithium metal batteries that employ high-voltage $LiNi_{0.8}Co_{0.15}Al_{0.05}O_2$ (NCA) cathodes. While the primary focus here is on solid-state batteries, our strategy for kaolinite liquid-phase exfoliation can serve as a scalable manufacturing platform for a wide variety of other kaolinite-based nanocomposite applications.

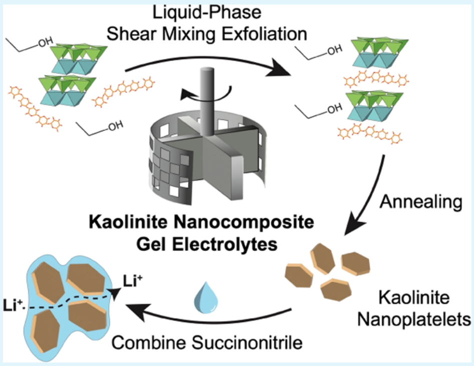

KEYWORDS: *clay nanocomposite, succinonitrile, liquid-phase exfoliation, solid-state battery, sustainability*

1. INTRODUCTION

Lithium-ion batteries (LIBs) have emerged as the leading technology for the portable electronics, transportation, and grid-level energy storage markets.[1] However, current commercial LIBs are reaching practical limitations in their energy density and are susceptible to catastrophic failure resulting from the use of flammable liquid electrolytes.[2,3] As a result, significant effort has been devoted to developing solid-state electrolytes (SSEs) that can resolve both challenges.[4,5] In particular, SSEs constructed with nonflammable constituents can significantly improve cell safety compared to traditional carbonate-based liquid electrolytes.[3,6] Moreover, SSEs that enable stable operation of next-generation negative electrodes, such as lithium metal, have the potential to provide significantly higher energy density than traditional LIBs.[4,7,8] However, currently available SSEs employ materials that are cost-prohibitive or not earth-abundant, limiting their manufacturing scalability and environmental sustainability.[9−12]

Clay-based nanocomposite electrolytes offer an enticing route to solid or quasi-solid electrolytes since they utilize earth-abundant and environmentally friendly clay materials that are geographically well distributed.[13,14] In addition, clays provide several desirable characteristics in an electrolyte matrix including high thermal stability, low electrical conductivity, and wide electrochemical stability window. Furthermore, when exfoliated, their structured aluminosilicate layers provide high gravimetric surface area that results in robust nanocomposite mechanical properties.[15] The most common clays utilized are montmorillonite, vermiculite, and halloysite for nanofillers or matrices in polymer,[16−21] polymer gel,[22−27] and ionogel[28−33] electrolytes. In these cases, the nanoclay provides mechanical support, increasing the electrolyte mechanical modulus and decreasing polymer crystallinity that enhances ionic conductivity.[16,27] Despite the breadth of demonstrated clay nanocomposite electrolytes, the most naturally abundant clay

Received: March 10, 2024
Revised: June 4, 2024
Accepted: June 11, 2024
Published: June 26, 2024

https://doi.org/10.1021/acsami.4c03997

variety, kaolinite, has rarely been utilized.[14,34] The 1:1 structure of silica and alumina layers within bulk kaolinite results in strong hydrogen bonding between the layers making exfoliation difficult relative to other clay varieties.[14,15] Although kaolinite nanocomposites produced through chemical intercalation have been demonstrated, this process is time-intensive and limited to a small subset of molecules, restricting potential applications.[35,36] Only one reported system to date has shown direct liquid-phase exfoliation of kaolinite, albeit with the assistance of a large fraction of graphene oxide (GO) dispersing agent (i.e., 5:1 GO/kaolinite) and no reported yield for the process.[37,38] Therefore, a need remains for a highly scalable kaolinite exfoliation process that will enable broader use of kaolinite in SSEs and related clay nanocomposite applications.

Herein, we report the fabrication of a gel electrolyte using kaolinite nanoplatelets (KNPs) produced via scalable liquid-phase exfoliation. The exfoliation process uses a low loading of ethyl cellulose (EC) dispersant (<0.5:1 EC/kaolinite) to achieve efficient extraction of KNPs from bulk kaolinite. The KNPs produced via this process exhibit a high specific surface area relative to bulk kaolinite, which facilitates strong gelation with liquid electrolytes at low mass loadings. Specifically, when KNPs are mixed with a succinonitrile (SN) liquid electrolyte, the resulting gel electrolyte possesses a range of superlative properties including high room-temperature ionic conductivity (1 mS cm^{-1}), stiff storage modulus (>10 MPa), wide electrochemical stability window (4.5 V vs Li/Li^+), and excellent thermal stability (>100 °C). These desirable attributes are exploited in lithium metal batteries (LMB) using $LiFePO_4$ (LFP) or $LiNi_{0.8}Co_{0.15}Al_{0.05}O_2$ (NCA) positive electrodes paired with a thin (<50 μm) lithium metal negative electrode. These solid-state LMBs achieve excellent performance, particularly >56% capacity utilization up to a current density of 2 mA cm^{-2}. Furthermore, the cycling stability of these solid-state LMBs was tested using a charge/discharge current density of 0.5 mA cm^{-2} with both LFP and NCA cell types producing lifetimes exceeding 125 cycles. Overall, this work establishes a scalable and sustainable approach for producing KNPs for solid-state LMBs and other kaolinite-based nanocomposite applications.

2. MATERIALS AND METHODS

2.1. Exfoliation of Kaolinite Clay. Bulk kaolinite (natural, Sigma-Aldrich) was exfoliated using liquid-phase shear mixing. The as-received bulk kaolinite (120 g) was mixed with ethanol (800 mL, 200 proof, Fisher Scientific) and various amounts of ethyl cellulose (EC) (12−60 g, 4 cP viscosity grade, Sigma-Aldrich) in a jacketed beaker with cooling water at 7 °C running through the jacket space. The mixture was shear-mixed at 10,230 rpm for 4 h (LMA-5, Silverson Machines) using a high-shear stator screen with square holes. The resulting mixture was then size-separated using a centrifuge (J-26 XPI, Beckman Coulter) at 4000 rpm (r_{max} = 3000 x g) for 20 min. The supernatant containing the nanoplatelets was flocculated using deionized (DI) water at a 64:39 mass ratio (supernatant: DI water). The flocculated mixture was centrifuged at 7500 rpm (r_{max} = 10,400 x g) for 6 min after which the sediment was collected and dried at 120 °C for 4 h. The dried powder was annealed in air at 400 °C for 4 h to remove the remaining EC, resulting in a partial coating of oxidized amorphous carbon on the surface of the kaolinite nanoplatelets (KNPs).

2.2. Preparation of SN Liquid Electrolyte. Succinonitrile (SN) (Thermo Fisher Scientific, 98%) was purified by solvent extraction in boiling diethyl ether. An insoluble and yellow-colored impurity remained after extraction and decanting. The extracted SN was then recrystallized in diethyl ether followed by drying under vacuum at 50 °C for 12 h. Purified SN was combined with 0.5 M $LiBF_4$ (99.99%, Sigma-Aldrich), 0.5 M LiTFSI (99.95%, Sigma-Aldrich), and 20 vol % fluoroethylene carbonate (FEC) (>99%, anhydrous, Sigma-Aldrich), after which the mixture was magnetically stirred at 60 °C for 2 h and stored under an inert argon environment.

2.3. Characterization of KNP and KNP-SN Electrolyte Gel. Micrographs of bulk kaolinite (as-received), annealed KNP powder, and KNP-SN gel were taken using a scanning electron microscope (SEM) (SU8030, Hitachi). Powder samples were dispersed in isopropanol, bath-sonicated, and drop-cast onto a silicon wafer prior to imaging. Gel samples were manually deposited via a spatula onto carbon tape for imaging. Fourier transform infrared spectroscopy (FTIR; Nexus 870, Thermo Nicolet) spectra of KNP, SN liquid electrolyte components, and KNP gels were taken at various compositions using attenuated total reflectance (ATR) over the range of 600−4000 cm^{-1} to determine the interactions between various components of the electrolyte. Atomic force microscopy (AFM) (Asylum Research Cypher, Oxford Instruments) was performed on the exfoliated KNPs to determine the lateral size and thickness of the nanoplatelets using the same powder sample preparation described above. Scanning transmission electron microscopy (S/TEM) (JEOL, ARM200) operating at 200 kV coupled with energy-dispersive spectroscopy (EDS) (Thermo Fisher, Dual SDD EDS (1.7 sr)) was used to obtain TEM micrographs and EDS mapping. The powder samples were bath-sonicated in isopropanol solvent and drop-cast on lacey carbon grid (300 mesh, Ted Pella) for this characterization. The convergent angle and collection angles for ADF-STEM imaging are 25 and 90−250 mrad, respectively. Data acquisition and processing (background subtraction and principal component analysis for denoising and chemical mapping) was conducted using Gatan GMS software. X-ray photoelectron spectroscopy (XPS) (Thermo Scientific, ESCALAB 250Xi XPS) was performed on the exfoliated KNPs. The spectrometer was equipped with a monochromated Al Kα X-ray source with 1486.6 eV energy. The XPS measurement spot size was ∼500 μm, and a flood gun was utilized for charge compensation. The XPS data analysis was performed using Avantage (Thermo Scientific) software where peaks were charge-corrected to adventitious carbon (C 1s) at 284.8 eV. X-ray diffraction (XRD) (Smartlab, 3 kW Gen2, Rigaku) was performed on both the bulk kaolinite and the annealed KNP. The θ−2θ XRD scans used a copper source ($K\alpha_{,avg}$ = 1.541874 Å) at a tube current and accelerating voltage of 35 mA and 40 kV, respectively. The data was collected in one-dimensional (1D) mode using a 2D HyPix-3000 in X-ray fluorescence (XRF) reduction mode. Nitrogen physisorption isotherms were performed on both the bulk kaolinite and the annealed KNPs, with 0.3 g of each sample dried at 120 °C under vacuum (VacPrep, Micrometrics) for >16 h until the rate of pressure change was below 0.001 mmHg min^{-1} prior to analysis. N_2 adsorption and desorption isotherms were then collected (3Flex, Micromeritics) at the normal boiling temperature of liquid nitrogen, and the surface area was calculated using the Brunauer−Emmett−Teller (BET) equation with embedded software (Micrometrics). The KNP-SN gel was produced by combining the KNP powder with SN liquid electrolyte in the desired mass ratio (i.e., KNP(x%)-SN) followed by mixing via mortar and pestle to produce the gel electrolyte. Rheology of the various KNP gels produced was measured using a rheometer (MCR 302, Anton Parr) at 25 °C with a parallel plate configuration (8 mm diameter), 1.0 mm gap, fixed 0.1% strain, and frequency sweep from 10^{-1} to 10^2 rad s^{-1}. Thermogravimetric analysis (TGA/DSC 3+, Mettler Toledo) was performed on KNP-EC mixtures, annealed KNP, SN liquid electrolyte, and KNP-SN gels using a nitrogen environment and a heating rate of 10 °C min^{-1} from 25 to 800 °C. A flame test was administered on both a KNP(45%)-SN gel and a traditional carbonate liquid electrolyte (1 M $LiPF_6$ in 1:1 EC/DEC (v/v)) by dosing 100 mg of either electrolyte onto a glass fiber separator (Whatman, GF/F, 2 cm diameter) and applying a propane torch flame to the sample for 1 s before being removed and observing the resulting reaction.

https://doi.org/10.1021/acsami.4c03997
ACS Appl. Mater. Interfaces 2024, 16, 34913−34922

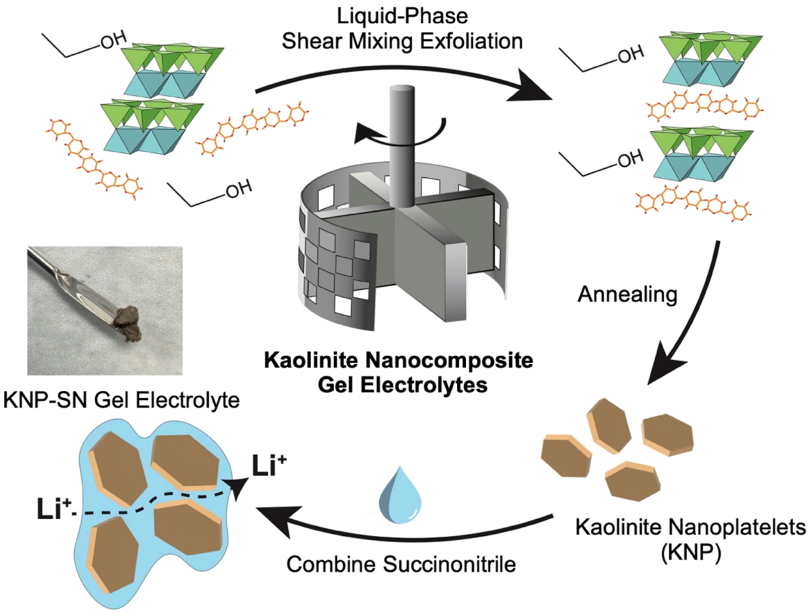

Figure 1. Schematic illustration of kaolinite nanoplatelet (KNP) electrolyte production including liquid-phase exfoliation of natural kaolinite with ethanol and ethyl cellulose (EC) using a high-shear radial mixer producing exfoliated KNPs; high-temperature annealing to remove residual EC; KNP gel electrolyte synthesis with a succinonitrile (SN) liquid electrolyte.

2.4. Electrode Preparation. The LFP and NCA positive electrodes were prepared using either $LiFePO_4$ (MTI, EQ-Lib-LFPO-S21) or $LiNi_{0.8}Co_{0.15}Al_{0.05}O_2$ (BASF TODA) along with carbon black (MTI, EQ-Lib-SuperC45), poly(vinylidene difluoride) (PVDF) (MTI, EQ-Lib-PVDF), and purified SN mixed with LiTFSI at a molar ratio of 20:1 (SN:LiTFSI). The above components were mixed with NMP at ∼50 wt % at a ratio of 80:10:5:5 (active material: SN:CB:PVDF) to make a slurry that was blade-coated on carbon-coated aluminum foil (MTI, EQ-CC-Al-18u-260). The coated electrodes were initially dried at 80 °C for 30 min, followed by further drying under vacuum at 50 °C for 12 h. The dried electrodes were cut into 10 mm disks and calendared through a gap of 50−60 μm. Positive electrode disks used for rate testing contained an active material loading of 10−11 mg cm^{-2}, while electrode disks used for cycle stability testing contained 5−6 mg cm^{-2}. The lithium metal negative electrodes (China Energy Lithium Co., >99.9%) were cut into 12.7 mm diameter disks and had a final thickness of <50 μm.

2.5. Electrochemical Characterization. Ionic conductivity (σ) of the KNP-SN gels was determined using electrochemical impedance spectroscopy (EIS) (VSP, BioLogic) with coin cells (CR2032) constructed with a stainless steel (SS)| KNP-SN|SS geometry. The ionic conductivity was determined according to the following equation, $\sigma = \frac{t}{R \times A}$, where t and A are the thickness and cross-sectional area of the KNP-SN gel, respectively, and R is the bulk impedance as measured by EIS (10 mV amplitude, 1 MHz−1 Hz). The temperature of the EIS coin cells was controlled by an environmental chamber (BTX-475, Espec). Lithium transference number (T_{Li}) was measured by the Bruce−Vincent method.[39] A coin cell with Li|Li symmetric structure was constructed, and a constant bias (ΔV) of 10 mV was applied for 2 h after which the current was recorded and an EIS measurement was performed before and after polarization. The lithium transference number was determined by the following equation: $T_{Li} = \frac{I_S(\Delta V - I_0 R_0)}{I_0(\Delta V - I_S R_S)}$, where I_S/I_0 are the steady state and initial measured currents, and R_S/R_0 are the steady state and initial interfacial impedance as measured by EIS. Cyclic voltammetry (CV) was performed using an SS|Li coin cell configuration where the SS electrode was swept between −0.2 and 3.0 V at a rate of 1 mV s^{-1} to probe the cathodic stability of the electrolyte. To determine oxidative stability, chronoamperometry (CA) was performed using an NCA|Li coin cell structure, where the cell was charged in 0.1 V increments with a voltage hold for 12 h while the leakage current was recorded. Additionally, linear sweep voltammetry (LSV) was performed using an SS|Li cell configuration where the voltage was increased from OCV to 6 V vs Li/Li^+ at 1 mV s^{-1}. The cycling stability of lithium plating and stripping was measured using a Li|KNP(45%)-SN gel|Li coin cell with 1 h plate/strip intervals at a current density of 0.2 mA cm^{-2}.

2.6. Battery Cell Cycling. KNP(45%)-SN gel was applied manually via a spatula and razor blade to the positive electrode disks (LFP or NCA). The final thickness of the gel was measured with a micrometer to be 200−300 μm. The coated positive electrode was combined with the lithium metal negative electrode and assembled into a CR2032 coin cell. All coin cell construction was performed inside an argon-filled glovebox. All galvanostatic cycling was performed using a battery cycling system (BT-2143, Arbin) at room temperature (22 °C) or elevated temperature (60 °C). LFP|Li cells were cycled between 2.5 and 4.0 V with 1C = 170 mA g^{-1}. NCA|Li cells were cycled between 2.5 and 4.3 V with 1C = 200 mA g^{-1}. Cells undergoing rate performance testing underwent no initial formation cycles. Cells undergoing cycling stability testing underwent two formation cycles. LFP|Li cells were conditioned using a pulsed charging method (0.5 mA cm^{-2} charge, 15 s on/90 s off, 0.5 mA cm^{-2} constant-current discharge) with a charge capacity limit for the first cycle (Figure S22). NCA|Li cells underwent one CCCV cycle at 0.1C charge/discharge with a voltage hold at 4.3 V followed by a second cycle using the same pulsed charging method.

3. RESULTS AND DISCUSSION

3.1. Liquid-Phase Exfoliation and Characterization of Kaolinite Nanoplatelets.

Figure 1 contains a schematic that depicts the preparation of KNP gel electrolytes from bulk kaolinite and liquid SN electrolyte. The exfoliation of bulk kaolinite to produce KNPs was executed using shear mixing in ethanol with EC added as a dispersing agent to minimize reagglomeration of the aluminosilicate layers. The addition of EC to the shear-mixing suspension greatly improves the process yield with an approximately linear relationship observed between the KNP yield and the starting ratio of EC to bulk kaolinite (Figure S1). After shear mixing, the dispersion is centrifuged to sediment and remove unexfoliated

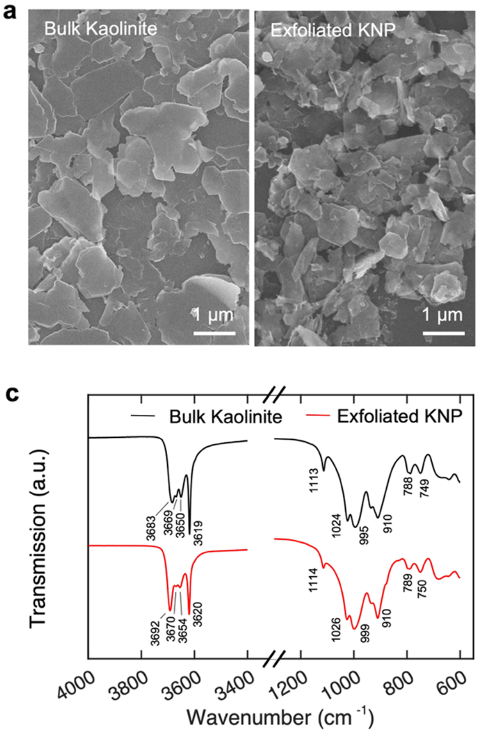

Figure 2. Characterization of kaolinite nanoplatelets (KNPs). (a) Scanning electron microscopy (SEM) images of bulk kaolinite and exfoliated KNP powders. (b) X-ray diffraction (XRD) of bulk kaolinite and exfoliated KNP powders, where the characteristic reflections of kaolinite (●) and quartz impurity (■) are marked. Table S1 lists the peaks and associated interplanar spacing for both diffraction patterns. (c) FTIR spectra of bulk kaolinite and exfoliated KNP powders. Full spectra and peak assignments are provided in Figure S8 and Table S2. (d) Nitrogen isotherms of bulk kaolinite and exfoliated KNP powders with the reported Brunauer−Emmett−Teller (BET) surface area. The BET analysis parameters are provided in Table S3.

bulk kaolinite, which is then recovered for subsequent exfoliation. Recycling this sediment generates an increase in yield of ∼20% compared to using fresh bulk kaolinite alone even when accounting for residual EC in the sediment. The centrifugation supernatant that contains KNPs is flocculated with deionized water, collected, and dried. The flocculated KNP is then annealed to decompose and volatilize excess EC (Figure S2), partially coating KNP in a nonconductive oxidized amorphous carbon coating, which gives the final powder a brownish color. The coating appears as a dark band along the KNP edges in transmission electron microscopy (TEM) (Figure S3) and is further confirmed by X-ray photoelectron spectroscopy (XPS) (Figure S4) as well as energy-dispersive X-ray spectroscopy (EDS) at the KNP edge (Figure S5a,b). Following the exfoliation and annealing steps, the resulting KNP powder can be readily dispersed with a liquid electrolyte such as SN to yield a high-performance gel electrolyte.

Characterization of the KNPs produced by EC-based liquid-phase exfoliation via scanning electron microscopy (SEM) (Figure 2a) and TEM (Figure S6) shows a hexagonal plate-like morphology. Comparison of the SEM micrographs before and after exfoliation reveals a decrease in average lateral size that is then further quantified by atomic force microscopy (AFM) to reveal an average lateral size and thickness of 190 ± 50 and 17 ± 5 nm, respectively (Figure S7). AFM also reveals that the distribution of nanoplatelet thicknesses has a median thickness of 3 nm, which is equivalent to ∼4 kaolinite layers (∼0.7 nm per layer). To validate this result, powder X-ray diffraction (XRD) was employed to compare the structure of bulk kaolinite and KNP. Both diffractograms exhibit the characteristic reflections of kaolinite marked in Figure 2b and listed in Table S1.[40] Specifically, the diffraction pattern of bulk kaolinite exhibits strong characteristic peaks at $2\theta = 12.25°$ ($d_{001} = 7.23$ Å) and $2\theta = 24.75°$ ($d_{002} = 3.60$ Å), corresponding to the basal planes of the silica tetrahedral and alumina octahedral sheets.[37,40] In contrast, the XRD diffraction pattern for exfoliated KNPs shows significantly diminished (001), (002), and (003) reflections when compared to the (020) reflection, thereby verifying a significant disruption of the stacking periodicity of kaolinite layers following exfoliation.

To ensure that the KNP exfoliation process does not degrade the kaolinite structure, FTIR was utilized (Figure 2c) with peak assignments being made according to reported spectral studies (Figure S8, Table S2).[41,42] The KNPs maintain the three characteristic hydroxyl peaks along the interlayer surface (3692, 3670, and 3654 cm^{-1}) as well as the sharp peak at 3620 cm^{-1} representing the inner hydroxyl stretching mode. Similarly, peaks at 1114, 1026, and 999 cm^{-1} representing the Si−O vibrational modes are also present. It is notable that a blue shift in vibrational frequency is seen in the hydroxyl and Si−O peaks of the KNP spectra compared to bulk kaolinite, while the Al−OH band (910 cm^{-1}) remains consistent. This observation has been previously reported and attributed to the accumulation of structural defects in KNP along the Si−O and hydroxyl surfaces during exfoliation while the alumina octahedron remains mostly unaffected.[37] All peaks in the KNP spectrum can be mapped to the bulk kaolinite structure with the exception of a broad peak at 1440 cm^{-1}, which can be attributed to the C−O and C−H stretching from the annealed EC on the nanoplatelet surface.

To further characterize the resulting KNPs, nitrogen adsorption isotherms were measured, revealing that the

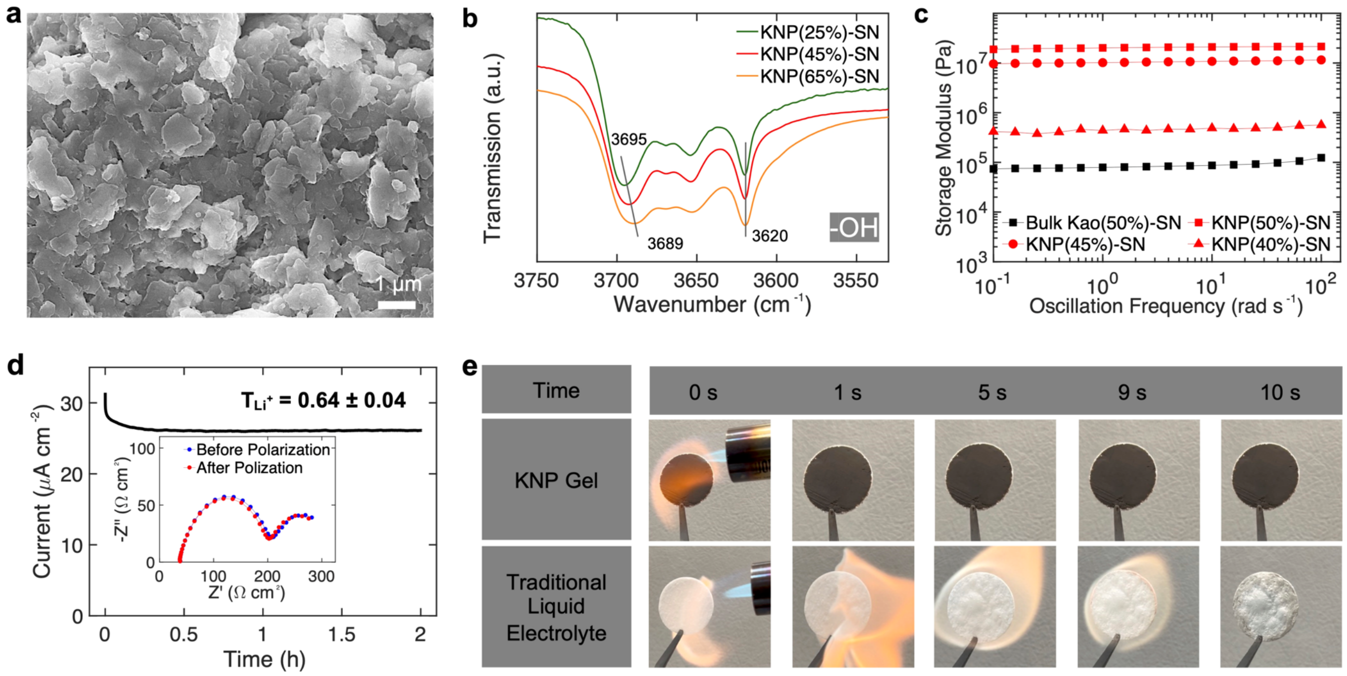

Figure 3. Kaolinite nanoplatelet (KNP)-succinonitrile (SN) gel electrolyte. (a) Scanning electron microscopy (SEM) image of the KNP-SN gel. (b) FTIR spectra of the hydroxyl vibrational bands of KNP-SN gel electrolytes showing a blue shift of interlayer hydroxyl groups as additional liquid electrolyte is added. (c) Rheological properties of the KNP-SN gel electrolyte at different loadings of KNP compared to a bulk kaolinite−SN gel. (d) Chronoamperometry (CA) and electrochemical impedance spectroscopy (EIS) of a Li|Li cell were used to determine the lithium transference number (T_{Li}) of the KNP-SN gel. (e) Flame test comparison of the KNP-SN gel and a traditional liquid electrolyte on a 2 cm diameter glass fiber separator.

Brunauer−Emmett−Teller (BET) surface area more than doubled from 9.7 to 24 $m^2\ g^{-1}$ following kaolinite exfoliation (Figure 2d, Table S3). The lack of hysteresis in the nitrogen adsorption isotherms coupled with direct observations of the KNP morphology via SEM suggests the absence of kaolinite nanoscrolls unlike previously reported kaolinite exfoliation methods.[35,37] This elimination of kaolinite nanoscrolls in our exfoliated samples can be attributed to the smaller lateral size of our KNPs, which suppresses rolling of the layers and results in higher gravimetric surface area than previous reports with extensive kaolinite nanoscrolls.[37]

3.2. Characterization of Kaolinite Gel Electrolyte. To test the utility of the KNPs, they were mixed with a SN liquid electrolyte to produce a KNP-SN gel electrolyte denoted as KNP(x%)-SN, where x is the mass percent of KNP. SN has many advantages as an electrolyte including high thermal stability (T_b = 266 °C), high ionic conductivity (>1 mS cm^{-1}), and high oxidative stability.[43] Moreover, similar to kaolinite, SN is made from earth-abundant materials and is already mass-produced, facilitating its scalable use. To improve the stability of SN with lithium metal, SN was mixed with two lithium salts (lithium bis(trifluoromethanesulfonyl)imide (LiTFSI) and lithium tetrafluoroborate ($LiBF_4$)) along with a film-forming additive, fluoroethylene carbonate (FEC), similar to other reported SN electrolytes.[44−47] Figure 3a shows an SEM micrograph of the resulting KNP-SN gel electrolyte, revealing the confinement of the liquid component along the contours of the nanoplatelets. The interaction between the KNP and liquid electrolyte phase is validated by FTIR as a blue shift of the interlayer hydroxyl group (Figure 3b) and Si−O (Figure S9) vibrational bands as the relative SN content increases. As expected, the inner hydroxyl group peak at 3920 cm^{-1} is unaffected by the electrolyte composition. These favorable interactions result in a high storage modulus (>10 MPa) of the KNP-SN gel, which enables its use as both an electrolyte and separator within LMB cells by preventing short-circuiting and inhibiting lithium dendrite growth (Figure 3c). In contrast, equivalent SN gel electrolytes made with bulk kaolinite showed a storage modulus that was over 2 orders of magnitude lower due to the lower surface area for interaction. The quasi-solid nature of the KNP-SN gel is further confirmed by the storage modulus being consistently higher than the loss modulus across a wide range of shear frequencies (Figure S10).

In addition to excellent mechanical properties, the KNP-SN gel possesses a high ionic conductivity of 1 mS cm^{-1} at 20 °C (Figure S11, Table S4), which is comparable to the SN component alone, enabling high rate capability in LMB cells.[43] Furthermore, Figure 3d shows the lithium transference number (T_{Li}) of the KNP-SN gel electrolyte extracted using the Bruce−Vincent method.[39] The plot displays the chronoamperometry as a 10 mV bias is applied to the Li|Li cell. The inset shows the EIS Nyquist plot before and after polarization where two semicircles are evident representing the interfacial and charge transfer resistances (Figure S12). The calculated T_{Li} for the KNP-SN gel electrolyte is 0.64 ± 0.04, which is significantly higher than that measured for the SN liquid electrolyte alone (0.49 ± 0.03, Figure S12), displaying an additional advantage of the KNP-SN gel electrolyte. To investigate this point further, FTIR was employed to compare various KNP compositions in the electrolyte (Figure S13). Figure S13a shows the blue shifting of the peak associated with the asymmetric stretching of the $-CF_3$ groups within the TFSI anion (~1191 cm^{-1}) as KNP content is increased.[48] This shift is likely due to hydrogen bonding with exposed hydroxyl groups on the surface of the KNP. A similar hydrogen bonding is also likely occurring with the carbonyl group of FEC as

https://doi.org/10.1021/acsami.4c03997
ACS Appl. Mater. Interfaces 2024, 16, 34913−34922

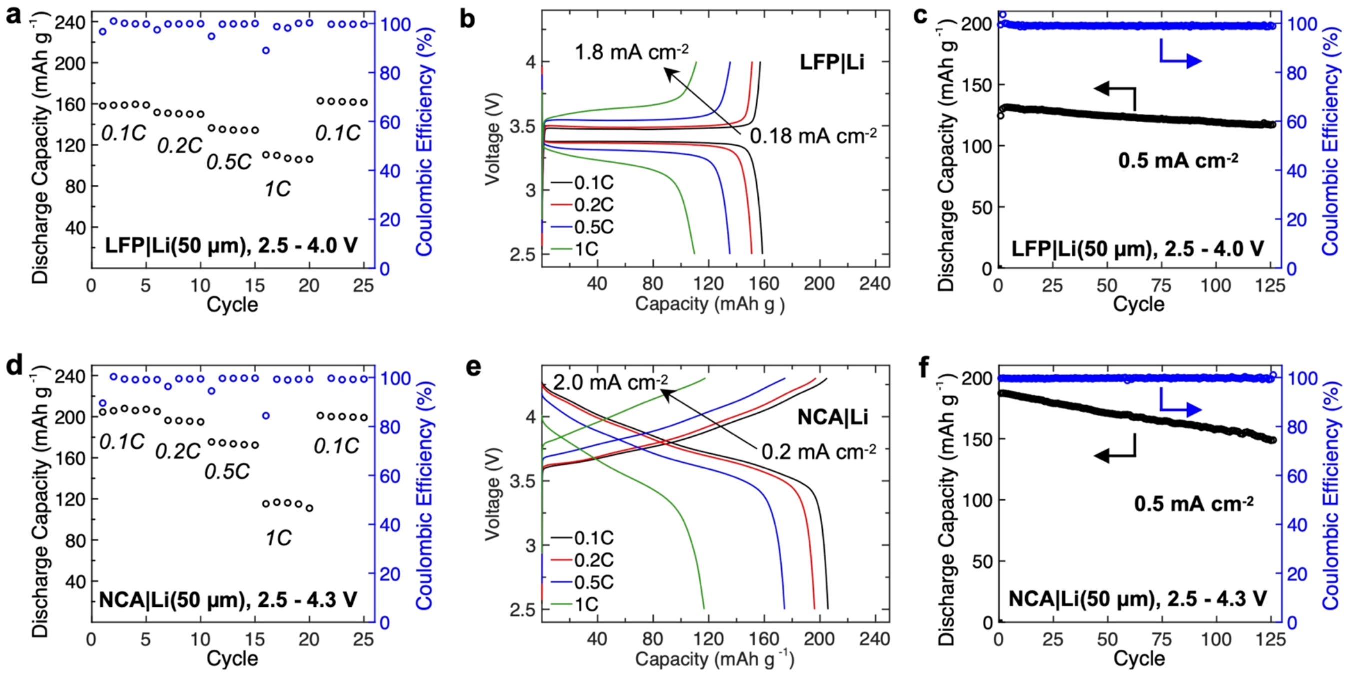

Figure 4. Electrochemical performance of the KNP-SN gel electrolyte in lithium metal battery cells at room temperature (22 °C). (a, d) Rate capability of LFP/NCA|Li cells with KNP(45%)-SN gel electrolyte at various charge/discharge rates and (b, e) the corresponding voltage profiles. The active material loading for the LFP and NCA cells used for rate testing is 10−11 mg cm^{-2}. (c, f) Cycle stability performance of LFP/NCA|Li cells with KNP(45%)-SN gel electrolyte at 0.5 mA cm^{-2} charge/discharge rate and 5−6 mg cm^{-2} active material loading.

evidenced by a blue shift in the stretching peaks (∼1830 and ∼1806 cm^{-1}) accompanied by a change in relative intensity of the two modes (Figure S13b). Furthermore, Figure S13c shows nitrile stretching peaks (∼2254 and ∼2277 cm^{-1}), which previous studies have assigned to bulk SN and SN bound to the Li$^+$ cation, respectively.[49] As the KNP loading increases, the relative area of the SN-Li$^+$ peak decreases, indicating that lithium is being solvated by other species, likely the exposed silica surface of the KNPs, which has been demonstrated in other clay-based electrolytes.[17−19,21,23] It appears likely that the combined effect of Li salt interactions with the KNP surface accounts for the increase in lithium transference number of the KNP-SN gel compared to the SN-only liquid electrolyte. It should be noted that an analysis of the BF$_4$ anion environment is obscured due to the overlap of the peak assigned to the BF$_4$ stretch at ∼1028 cm^{-1} and the Si−O stretch of the KNPs (Figures S14 and S15).[50] Additionally, regarding the partial coating of oxidized amorphous carbon on the KNPs, the low concentration and corresponding low spectral intensity preclude detailed FTIR analysis. Nevertheless, to eliminate concerns of electrical conductivity from the oxidized amorphous carbon on the KNPs, chronoamperometry (Figure S16) was performed on the KNP-SN gel electrolyte and revealed a measured conductivity of 6.30 × 10^{-10} S cm^{-1}, which is sufficiently insulating for SSEs in energy storage applications.

To further assess the compatibility of the KNP-SN gel electrolyte for energy-dense LMBs, the electrochemical stability window was evaluated at both high and low potentials relative to Li/Li$^+$. Utilizing linear sweep voltammetry (LSV) in an SS|Li cell configuration, the oxidative stability limit of the KNP-SN gel was shown to be higher than that of the SN liquid electrolyte alone (Figure S17a). The SN liquid electrolyte showed an indication of reaction at ∼4.7 V vs Li/Li$^+$, which agrees with previous reports on the anodic stability limit of FEC.[45] However, LSV has been known to overestimate electrochemical stability limits depending on the working electrode material.[51] Therefore, chronoamperometry (CA) was used to more accurately determine the oxidative stability limit of the KNP-SN gel (Figure S17b). In particular, an NCA|Li cell with KNP(45%)-SN or SN liquid electrolyte was charged in 0.1 V increments with 12 h voltage holds where the leakage current was measured at each step. In the case of the SN liquid electrolyte, the leakage current began significantly increasing step-overstep above 4.2 V vs Li/Li$^+$, which indicates the onset of deleterious side reactions from electrolyte breakdown. In contrast, in agreement with the trend found in LSV, leakage current from the KNP(45%)-SN gel did not increase step-overstep until 4.6 V vs Li/Li$^+$. Thus, the oxidative stability limit of the KNP(45%)-SN gel is at least 4.5 V vs Li/Li$^+$, which is sufficient for many high-voltage and energy-dense positive electrodes. To test the stability with a lithium metal negative electrode, cyclic voltammetry (CV) was executed between −0.2 and 3.0 V using a stainless steel (SS) blocking electrode paired with Li metal (Figure S18). The KNP(45%)-SN gel voltammogram shows consistent overpotentials and peak currents after seven cycles with the anodic and cathodic peak currents remaining roughly equal in magnitude, indicating a high coulombic efficiency and suggesting that surface layers have been sufficiently formed to inhibit further deleterious reactions. By comparison, the SN liquid electrolyte voltammogram shows increasing and then decreasing peak currents with apparent stability and equal anodic and cathodic currents achieved after 10 cycles. To further validate the stability of KNP-SN gels against lithium metal, Li|KNP(45%)-SN|Li symmetric cells were constructed and cycled at 0.2 mA cm^{-2} with 1 h cycles, revealing stable operation for over 400 h as shown in Figure S19.

Since thermal stability and safety are key factors for LMB electrolytes, the thermal stability of the KNP-SN gel and its components were measured using thermogravimetric analysis (TGA) (Figure S20). The annealed KNP powder has excellent thermal stability with measurable mass loss only detectable at temperatures exceeding ∼500 °C, where it is known that dehydroxylation of the kaolinite structure occurs.[52] The KNP-SN gel reaches 2% mass loss at 100 °C ($T_{2\%}$), which represents significantly higher thermal stability than traditional carbonate electrolytes.[53] To validate this result, Figure 3e shows flame test results comparing the flammability of the KNP-SN gel electrolyte compared to a traditional carbonate liquid electrolyte (1 M $LiPF_6$ in 1:1 EC/DEC (v/v)). The same mass of each electrolyte was supported on separate glass fiber separators, after which a torch was applied to the sample for the same length of time. In the case of the KNP-SN gel, the sample was not ignited, whereas the carbonate electrolyte caught fire and burned until the electrolyte was fully consumed. The higher thermal stability of KNP-SN gels compared to traditional liquid electrolytes implies enhanced safety in LMB applications.

3.3. Lithium Metal Battery Performance with Kaolinite Gel Electrolyte. To test the LMB rate performance and cycling stability of the KNP-SN gel electrolyte, LFP|Li and NCA|Li cells were constructed using the KNP(45%)-SN gel as both the electrolyte and separator. Figure 4a,d shows the rate performance of these different cells. Using positive electrodes with high active material loading (>10 mg cm^{-2}), both cell types achieved high discharge capacities of 160 and 200 mAh g^{-1} at 0.1C (0.18−0.2 mA cm^{-2}) for LFP|Li and NCA|Li, respectively, which approach the practically achievable capacity of each chemistry. Furthermore, the cells maintained a discharge capacity of at least 115 mAh g^{-1} at a 1C rate (1.8−2.0 mA cm^{-2}) with >56% capacity utilization compared to 0.1C, which is considerable as this current density nears that of practical electric vehicle applications. The voltage profiles of both cell types (Figure 4b,e) appear as expected, with flat plateaus near ∼3.48 and ∼3.37 V for LFP|Li cells and a slope in voltage for NCA|Li cells, indicating stable electrochemical operation. The cycle stability of the LFP|Li and NCA|Li cells (Figure 4c,f) were tested with thin lithium metal (50 μm) at a charge/discharge current density of 0.5 mA cm^{-2}, which is equal to or higher than the reported stability testing of other SN electrolytes.[46,47,54−60] The positive electrode active material loading for cycle stability testing was chosen to be 5 mg cm^{-2} to expedite the testing time. Both cell types reached 125 cycles with a capacity retention of 94 and 80% for LFP|Li and NCA|Li, respectively, which is comparable to the performance of recently reported cycle stability testing of SN electrolytes (Table S5). Furthermore, the average coulombic efficiency of each cell type was >99.3% over the course of this testing. Given the high thermal stability of the KNP-SN gel electrolyte, the rate capability at 1C of both LFP|Li and NCA|Li cells was tested at 60 °C (Figure S21). Both cell types showed an improvement in rate of 12 and 22% for the LFP and NCA cells, respectively, displaying an additional advantage of the high thermal stability of the KNP-SN gel electrolyte. By combining state-of-the-art LMB cycling and rate performance metrics with enhanced thermal stability, safety, and earth-abundant raw materials, the KNP-SN gel electrolyte is a promising option for next-generation energy storage technologies.

4. CONCLUSIONS

In conclusion, we have developed a scalable method of kaolinite exfoliation to produce KNPs that can be combined with SN to create a high-modulus and thermally stable gel electrolyte for use in solid-state LMBs. The exfoliation of bulk kaolinite is achieved with liquid-phase shear mixing using ethanol/EC to produce nanoplatelets based on the most earth-abundant clay. The resulting KNP-SN gel electrolyte achieves a range of superlative properties including high room-temperature ionic conductivity (1 mS cm^{-1}), stiff storage modulus (>10 MPa), and excellent thermal stability (>100 °C). Additionally, the interaction of the electrolyte with the exposed KNP surface results in an increase of the lithium-ion transference number compared to the liquid electrolyte alone ($T_{Li} = 0.64 \pm 0.04$ versus 0.49 ± 0.03). Furthermore, the KNP-SN gel is electrochemically stable with lithium metal over a range of potentials up to 4.5 V vs Li/Li^+. This electrochemical stability was utilized in LMB cells with both LFP and NCA positive electrodes against thin (50 μm) lithium metal negative electrodes. The rate capability of the LMB cells was tested using thick (>10 mg cm^{-2} active material) positive electrodes, with both cell types achieving >56% capacity utilization up to a current density of 2 mA cm^{-2}. Additionally, the cycle stability of the LMB cells was tested using a charge/discharge current density of 0.5 mA cm^{-2} with both cell types achieving >125 cycles, which is comparable to other state-of-the-art SN electrolytes. Overall, this work provides a viable path for the scalable exfoliation of kaolinite clay into KNPs that are suitable for solid-state LMBs in addition to other clay nanocomposite applications.

■ ASSOCIATED CONTENT

Supporting Information

The Supporting Information is available free of charge at https://pubs.acs.org/doi/10.1021/acsami.4c03997.

Plot of exfoliation yield versus initial kaolinite/EC ratio; TGA of KNP-EC mixtures from centrifugation and KNP-SN gel; (S)TEM/EDS of the KNPs; XPS spectra of the KNPs; histogram of KNP lateral and vertical sizes as determined by AFM; XRD reflections; FTIR spectra of as-received kaolinite and KNP with table of assigned peaks; BET surface area parameters for bulk kaolinite and KNPs; FTIR spectra of KNP-gel electrolytes focusing on the Si−O and Al−OH vibrational bands; rheology of the KNP-SN gel (45% KNP); ionic conductivity of various KNP-SN compositions at a range of temperatures and the corresponding fit parameters of VFT model; lithium transference number measurement of SN liquid electrolyte only; FTIR spectra of KNP gel electrolytes focusing on CF_3, carbonyl, and nitrile vibrational bands; complete FTIR spectra of SN liquid electrolyte and its components as well as various compositions of KNP-SN gel electrolytes; chronoamperometry of SS|KNP-SN|SS cell to determine electrical conductivity; LSV and chronoamperometry of KNP-SN gel and SN liquid electrolyte alone for oxidative stability; cyclic voltammetry of the KNP-SN gel and SN liquid electrolyte alone for stability with lithium metal; Li|Li symmetric cycling performance of KNP-SN gel; TGA of KNP, KNP-SN gel, and SN liquid electrolyte; cell performance from recently reported SN-based electrolytes; comparison of rate capability of LFP|Li and NCA|

Li cells at room temperature and 60 °C; and example of pulsed charging conditioning of cells (PDF)

AUTHOR INFORMATION

Corresponding Author

Mark C. Hersam − *Department of Materials Science and Engineering, Northwestern University, Evanston, Illinois 60208, United States; Department of Chemistry and Department of Electrical and Computer Engineering, Northwestern University, Evanston, Illinois 60208, United States*; orcid.org/0000-0003-4120-1426; Email: m-hersam@northwestern.edu

Authors

Cory M. Thomas − *Department of Materials Science and Engineering, Northwestern University, Evanston, Illinois 60208, United States*

Davy Zeng − *Department of Materials Science and Engineering, Northwestern University, Evanston, Illinois 60208, United States*

Hsien Cheng Huang − *Department of Materials Science and Engineering, Northwestern University, Evanston, Illinois 60208, United States*

Thang Pham − *Department of Materials Science and Engineering, Northwestern University, Evanston, Illinois 60208, United States*

Carlos G. Torres-Castanedo − *Department of Materials Science and Engineering, Northwestern University, Evanston, Illinois 60208, United States*; orcid.org/0000-0002-4505-7970

Michael J. Bedzyk − *Department of Materials Science and Engineering, Northwestern University, Evanston, Illinois 60208, United States; Department of Physics and Astronomy and Applied Physics Program, Northwestern University, Evanston, Illinois 60208, United States*; orcid.org/0000-0002-1026-4558

Vinayak P. Dravid − *Department of Materials Science and Engineering, Northwestern University, Evanston, Illinois 60208, United States*; orcid.org/0000-0002-6007-3063

Complete contact information is available at: https://pubs.acs.org/10.1021/acsami.4c03997

Author Contributions

$^{\perp}$C.M.T. and D.Z. contributed equally to this work. H.C.H. provided support with various electrochemical measurements. T.P. performed (S)TEM and EDS experiments and analysis. C.G.T.-C. performed XPS, XRD, and analysis. M.J.B., V.P.D., and M.C.H. assisted with manuscript revisions and project supervision.

Notes

The authors declare no competing financial interest.

ACKNOWLEDGMENTS

This work was supported by the National Science Foundation Future Manufacturing Program (NSF CMMI-2037026), the Northwestern University Materials Research Science and Engineering Center (NSF DMR-2308691), and the Trienens Institute for Sustainability and Energy at Northwestern University. In addition, C.M.T. was supported by the National Science Foundation Graduate Research Fellowship under Grant No. DGE-1842165. D.Z. was supported by the Northwestern University McCormick Summer Undergraduate Research Award and the Meister Undergraduate Research Fund. Scanning and transmission electron microscopy, EDS, XPS, and FTIR analysis were performed in the NU*ANCE* facility at Northwestern University, which is supported by the Soft and Hybrid Nanotechnology Experimental (SHyNE) Resource (NSF ECCS-2025633), the Materials Research Science and Engineering Center (MRSEC) (NSF DMR-2308691), the State of Illinois, and Northwestern University. Rheometry and TGA were performed in the MatCI facility, which receives support from the Materials Research Science and Engineering Center (MRSEC) (NSF DMR-2308691). Physisorption measurements (BET) were performed in the React Engineering and Catalyst Testing (REACT) core facility at Northwestern University. XRD was performed in the Jerome B. Cohen X-Ray Diffraction Facility supported by the MRSEC program of the National Science Foundation (DMR-2308691)

REFERENCES

(1) Manthiram, A. An outlook on lithium ion battery technology. *ACS Cent. Sci.* **2017**, *3* (10), 1063−1069.

(2) Chu, S.; Cui, Y.; Liu, N. The path towards sustainable energy. *Nat. Mater.* **2017**, *16* (1), 16−22.

(3) Liu, K.; Liu, Y.; Lin, D.; Pei, A.; Cui, Y. Materials for lithium-ion battery safety. *Sci. Adv.* **2018**, *4* (6), No. eaas9820.

(4) Manthiram, A.; Yu, X.; Wang, S. Lithium battery chemistries enabled by solid-state electrolytes. *Nat. Rev. Mater.* **2017**, *2* (4), No. 16103.

(5) Zheng, F.; Kotobuki, M.; Song, S.; Lai, M. O.; Lu, L. Review on solid electrolytes for all-solid-state lithium-ion batteries. *J. Power Sources* **2018**, *389*, 198−213.

(6) Wang, Q.; Mao, B.; Stoliarov, S. I.; Sun, J. A review of lithium ion battery failure mechanisms and fire prevention strategies. *Prog. Energy Combust. Sci.* **2019**, *73*, 95−131.

(7) Betz, J.; Bieker, G.; Meister, P.; Placke, T.; Winter, M.; Schmuch, R. Theoretical versus practical energy: A plea for more transparency in the energy calculation of different rechargeable battery systems. *Adv. Energy Mater.* **2019**, *9* (6), No. 1803170.

(8) Randau, S.; Weber, D. A.; Kötz, O.; Koerver, R.; Braun, P.; Weber, A.; Ivers-Tiffée, E.; Adermann, T.; Kulisch, J.; Zeier, W. G.; Richter, F. H.; Janek, J. Benchmarking the performance of all-solid-state lithium batteries. *Nat. Energy* **2020**, *5* (3), 259−270.

(9) Tan, D. H. S.; Banerjee, A.; Chen, Z.; Meng, Y. S. From nanoscale interface characterization to sustainable energy storage using all-solid-state batteries. *Nat. Nanotechnol.* **2020**, *15* (3), 170−180.

(10) Xu, L.; Lu, Y.; Zhao, C.-Z.; Yuan, H.; Zhu, G.-L.; Hou, L.-P.; Zhang, Q.; Huang, J.-Q. Toward the scale-up of solid-state lithium metal batteries: The gaps between lab-level cells and practical large-format batteries. *Adv. Energy Mater.* **2021**, *11* (4), No. 2002360.

(11) Huang, K. J.; Ceder, G.; Olivetti, E. A. Manufacturing scalability implications of materials choice in inorganic solid-state batteries. *Joule* **2021**, *5* (3), 564−580.

(12) Duffner, F.; Kronemeyer, N.; Tübke, J.; Leker, J.; Winter, M.; Schmuch, R. Post-lithium-ion battery cell production and its compatibility with lithium-ion cell production infrastructure. *Nat. Energy* **2021**, *6* (2), 123−134.

(13) Lan, Y.; Liu, Y.; Li, J.; Chen, D.; He, G.; Parkin, I. P. Natural clay-based materials for energy storage and conversion applications. *Adv. Sci.* **2021**, *8* (11), No. 2004036.

(14) Dedzo, G. K.; Detellier, C. Clay minerals—ionic liquids, nanoarchitectures, and applications. *Adv. Funct. Mater.* **2018**, *28* (27), No. 1703845.

(15) Wypych, F.; de Freitas, R. A. Clay minerals: Classification, structure, and properties. In *Developments in Clay Science*; Elsevier, 2022; Vol. *10*, pp 3−35.

(16) Chua, S.; Fang, R.; Sun, Z.; Wu, M.; Gu, Z.; Wang, Y.; Hart, J. N.; Sharma, N.; Li, F.; Wang, D.-W. Hybrid solid polymer electrolytes

with two-dimensional inorganic nanofillers. *Chem. - Eur. J.* **2018**, *24* (69), 18180−18203.

(17) Zhu, Q.; Wang, X.; Miller, J. D. Advanced nanoclay-based nanocomposite solid polymer electrolyte for lithium iron phosphate batteries. *ACS Appl. Mater. Interfaces* **2019**, *11* (9), 8954−8960.

(18) Feng, J.; Ao, X.; Lei, Z.; Wang, J.; Deng, Y.; Wang, C. Hollow nanotubular clay composited comb-like methoxy poly(ethylene glycol) acrylate polymer as solid polymer electrolyte for lithium metal batteries. *Electrochim. Acta* **2020**, *340*, No. 135995.

(19) Lin, Y.; Wang, X.; Liu, J.; Miller, J. D. Natural halloysite nanoclay electrolyte for advanced all-solid-state lithium-sulfur batteries. *Nano Energy* **2017**, *31*, 478−485.

(20) Tang, W.; Tang, S.; Zhang, C.; Ma, Q.; Xiang, Q.; Yang, Y.-W.; Luo, J. Simultaneously enhancing the thermal stability, mechanical modulus, and electrochemical performance of solid polymer electrolytes by incorporating 2D sheets. *Adv. Energy Mater.* **2018**, *8* (24), No. 1800866.

(21) Zhang, Y.; Zhao, Y.; Gosselink, D.; Chen, P. Synthesis of poly(ethylene-oxide)/nanoclay solid polymer electrolyte for all solid-state lithium/sulfur battery. *Ionics* **2015**, *21* (2), 381−385.

(22) Zhu, M.; Lan, J.; Tan, C.; Sui, G.; Yang, X. Degradable cellulose acetate/poly-l-lactic acid/halloysite nanotube composite nanofiber membranes with outstanding performance for gel polymer electrolytes. *J. Mater. Chem. A* **2016**, *4* (31), 12136−12143.

(23) Jeon, Y. M.; Kim, S.; Lee, M.; Lee, W. B.; Park, J. H. Polymer-clay nanocomposite solid-state electrolyte with selective cation transport boosting and retarded lithium dendrite formation. *Adv. Energy Mater.* **2020**, *10* (47), No. 2003114.

(24) Deka, M.; Kumar, A. Electrical and electrochemical studies of poly(vinylidene fluoride)−clay nanocomposite gel polymer electrolytes for Li-ion batteries. *J. Power Sources* **2011**, *196* (3), 1358−1364.

(25) Shubha, N.; Prasanth, R.; Hoon, H. H.; Srinivasan, M. Dual phase polymer gel electrolyte based on non-woven poly(vinylidenefluoride-co-hexafluoropropylene)−layered clay nanocomposite fibrous membranes for lithium ion batteries. *Mater. Res. Bull.* **2013**, *48* (2), 526−537.

(26) Hwang, J. J.; Liu, H. J. Influence of organophilic clay on the morphology, plasticizer-maintaining ability, dimensional stability, and electrochemical properties of gel polyacrylonitrile (PAN) nanocomposite electrolytes. *Macromolecules* **2002**, *35* (19), 7314−7319.

(27) Prasanth, R.; Shubha, N.; Hng, H. H.; Srinivasan, M. Effect of nano-clay on ionic conductivity and electrochemical properties of poly(vinylidene fluoride) based nanocomposite porous polymer membranes and their application as polymer electrolyte in lithium ion batteries. *Eur. Polym. J.* **2013**, *49* (2), 307−318.

(28) Grishina, E. P.; Ramenskaya, L. M.; Kudryakova, N. O.; Vagin, K. V.; Kraev, A. S.; Agafonov, A. V. Composite nanomaterials based on 1-butyl-3-methylimidazolium dicianamide and clays. *J. Mater. Res. Technol.* **2019**, *8* (5), 4387−4398.

(29) Zhao, N.; Liu, Y.; Zhao, X.; Song, H. Liquid crystal self-assembly of halloysite nanotubes in ionic liquids: a novel soft nanocomposite ionogel electrolyte with high anisotropic ionic conductivity and thermal stability. *Nanoscale* **2016**, *8* (3), 1545−1554.

(30) Noskov, A. V.; Alekseeva, O. V.; Shibaeva, V. D.; Agafonov, A. V. Synthesis, structure and thermal properties of montmorillonite/ionic liquid ionogels. *RSC Adv.* **2020**, *10* (57), 34885−34894.

(31) Alekseeva, O. V.; Shibaeva, V. D.; Noskov, A. V.; Ivanov, V. K.; Agafonov, A. V. Enhancing the thermal stability of ionogels: Synthesis and properties of triple ionic liquid/halloysite/MCC ionogels. *Molecules* **2021**, *26* (20), No. 6198, DOI: 10.3390/molecules26206198.

(32) Mao, H.; Ding, Z. Electrolytes based on nano-2D interlayer structure of Al-pillared clays for solid-state lithium battery. *J. Mater. Sci.: Mater. Electron.* **2020**, *31* (16), 13874−13888.

(33) Kalaga, K.; Rodrigues, M.-T. F.; Gullapalli, H.; Babu, G.; Arava, L. M. R.; Ajayan, P. M. Quasi-solid electrolytes for high temperature lithium ion batteries. *ACS Appl. Mater. Interfaces* **2015**, *7* (46), 25777−25783.

(34) U.S. Geological Survey. Mineral Commodity Summaries 2023. DOI: 10.3133/mcs2023 (accessed Feb 1, 2023).

(35) Kuroda, Y.; Ito, K.; Itabashi, K.; Kuroda, K. One-step exfoliation of kaolinites and their transformation into nanoscrolls. *Langmuir* **2011**, *27* (5), 2028−2035.

(36) Detellier, C.; Letaief, S. Chapter 13.2 - Kaolinite−Polymer Nanocomposites. In *Developments in Clay Science*; Elsevier, 2013; Vol. *5*, pp 707−719.

(37) Huang, X.; Li, Y.; Yin, X.; Tian, J.; Wu, W. Liquid-phase exfoliation of kaolinite by high-shear mixer with graphite oxide as an amphiphilic dispersant. *Langmuir* **2019**, *35* (43), 13833−13843.

(38) Huang, X.; Wu, W. Research and application of graphite oxide-assisted high-gravity rotating bed liquid phase exfoliation of kaolinite. *Chem. Pap.* **2023**, *77* (2), 745−755.

(39) Evans, J.; Vincent, C. A.; Bruce, P. G. Electrochemical measurement of transference numbers in polymer electrolytes. *Polymer* **1987**, *28* (13), 2324−2328.

(40) Bailey, S. W. Chapter 1 − Structure of Layer Silicates. In *Crystal Structur of Clay Materials and their X-Ray Identification*, 2nd ed.; Minerological Society, 1984; pp 1−124.

(41) Madejová, J. FTIR techniques in clay mineral studies. *Vib. Spectrosc.* **2003**, *31* (1), 1−10.

(42) Bich, C.; Ambroise, J.; Péra, J. Influence of degree of dehydroxylation on the pozzolanic activity of metakaolin. *Appl. Clay Sci.* **2009**, *44* (3), 194−200.

(43) Alarco, P.-J.; Abu-Lebdeh, Y.; Abouimrane, A.; Armand, M. The plastic-crystalline phase of succinonitrile as a universal matrix for solid-state ionic conductors. *Nat. Mater.* **2004**, *3* (7), 476−481.

(44) Duncan, H.; Salem, N.; Abu-Lebdeh, Y. Electrolyte formulations based on dinitrile solvents for high voltage Li-ion batteries. *J. Electrochem. Soc.* **2013**, *160* (6), No. A838, DOI: 10.1149/2.088306jes.

(45) Zhang, Q.; Liu, K.; Ding, F.; Li, W.; Liu, X.; Zhang, J. Safety-reinforced succinonitrile-based electrolyte with interfacial stability for high-performance lithium batteries. *ACS Appl. Mater. Interfaces* **2017**, *9* (35), 29820−29828.

(46) Fu, C.; Ma, Y.; Lou, S.; Cui, C.; Xiang, L.; Zhao, W.; Zuo, P.; Wang, J.; Gao, Y.; Yin, G. A dual-salt coupled fluoroethylene carbonate succinonitrile-based electrolyte enables Li-metal batteries. *J. Mater. Chem. A* **2020**, *8* (4), 2066−2073.

(47) Zhang, Q.; Liu, K.; Ding, F.; Li, W.; Liu, X.; Zhang, J. Enhancing the high voltage interface compatibility of LiNi0.5Co0.2Mn0.3O2 in the succinonitrile-based electrolyte. *Electrochim. Acta* **2019**, *298*, 818−826.

(48) Kam, W.; Liew, C.-W.; Lim, J. Y.; Ramesh, S. Electrical, structural, and thermal studies of antimony trioxide-doped poly(acrylic acid)-based composite polymer electrolytes. *Ionics* **2014**, *20* (5), 665−674.

(49) Shen, Y.; Deng, G.-H.; Ge, C.; Tian, Y.; Wu, G.; Yang, X.; Zheng, J.; Yuan, K. Solvation structure around the Li+ ion in succinonitrile−lithium salt plastic crystalline electrolytes. *Phys. Chem. Chem. Phys.* **2016**, *18* (22), 14867−14873.

(50) Rajendran, S.; Kannan, R.; Mahendran, O. Ionic conductivity studies in poly(methylmethacrylate)−polyethlene oxide hybrid polymer electrolytes with lithium salts. *J. Power Sources* **2001**, *96* (2), 406−410.

(51) Méry, A.; Rousselot, S.; Lepage, D.; Dollé, M. A Critical Review for an Accurate Elecrochemical Stability Window of Solid Polymer and Composite Electrolytes. *Materials* **2021**, *14* (4), No. 3840, DOI: 10.3390/ma14143840.

(52) Izadifar, M.; Thissen, P.; Steudel, A.; Kleeberg, R.; Kaufhold, S.; Kaltenbach, J.; Schuhmann, R.; Dehn, F.; Emmerich, K. Comprehensive examination of dehyroxylation of kaolinite, and dickite: Experimental studies and density functional theory. *Clays Clay Miner.* **2020**, *68* (4), 319−333.

(53) Zhang, H.; Ma, X.; Lin, C.; Zhu, B. Gel polymer electrolyte-based on PVDF/fluorinated amphiphilic copolymer blends for high performance lithium-ion batteries. *RSC Adv.* **2014**, *4* (64), 33713−33719.

(54) Abouimrane, A.; Davidson, I. J. Solid electrolyte based on succinonitrile and LiBOB: Interface stability and application in lithium batteries. *J. Electrochem. Soc.* **2007**, *154* (11), No. A1031, DOI: 10.1149/1.2781305.

(55) Lv, P.; Li, Y.; Wu, Y.; Liu, G.; Liu, H.; Li, S.; Tang, C.; Mei, J.; Li, Y. Robust succinonitrile-based gel polymer electrolyte for lithium-ion batteries withstanding mechanical folding and high temperature. *ACS Appl. Mater. Interfaces* **2018**, *10* (30), 25384−25392.

(56) Liu, K.; Zhang, Q.; Thapaliya, B. P.; Sun, X.-G.; Ding, F.; Liu, X.; Zhang, J.; Dai, S. In situ polymerized succinonitrile-based solid polymer electrolytes for lithium ion batteries. *Solid State Ionics* **2020**, *345*, No. 115159.

(57) Bi, J.; Mu, D.; Wu, B.; Fu, J.; Yang, H.; Mu, G.; Zhang, L.; Wu, F. A hybrid solid electrolyte Li0.33La0.557TiO3/poly(acylonitrile) membrane infiltrated with a succinonitrile-based electrolyte for solid state lithium-ion batteries. *J. Mater. Chem. A* **2020**, *8* (2), 706−713.

(58) Han, D.; Wang, P.; Li, P.; Shi, J.; Liu, J.; Chen, P.; Zhai, L.; Mi, L.; Fu, Y. Homogeneous and fast Li-ion transport enabled by a novel metal-organic-framework-based succinonitrile electrolyte for dendrite-free Li deposition. *ACS Appl. Mater. Interfaces* **2021**, *13* (44), 52688−52696.

(59) Wang, J.; Yang, J.; Shen, L.; Guo, Q.; He, H.; Yao, X. Synergistic Effects of Plasticizer and 3D Framework toward High-Performance Solid Polymer Electrolyte for Room-Temperature Solid-State Lithium Batteries. *ACS Appl. Energy Mater.* **2021**, *4* (4), 4129.

(60) Lee, M. J.; Han, J.; Lee, K.; Lee, Y. J.; Kim, B. G.; Jung, K.-N.; Kim, B. J.; Lee, S. W. Elastomeric electrolytes for high-energy solid-state lithium batteries. *Nature* **2022**, *601* (7892), 217−222.